The Indonesian Throughflow Circulation Under Solar Geoengineering

Chencheng Shen[1] John C. Moore[1,2]* Heri Kuswanto[3,4] Liyun Zhao[1]

[1]State Key Laboratory of Earth Surface Processes and Resource Ecology, Faculty of Geographical Science, Beijing Normal University, Beijing 100875, China

[2]Arctic Centre, University of Lapland, Rovaniemi, Finland

[3]Center for Disaster Mitigation and Climate Change, Institut Teknologi Sepuluh Nopember, Surabaya, Indonesia.

[4]Department of Statistics, Institut Teknologi Sepuluh Nopember, Surabaya, Indonesia.

Correspondence to: john.moore.bnu@gmail.com, zhaoliyun@bnu.edu.cn

Short summary (less than 500 characters):

The Indonesia Throughflow is an important pathway connecting the Pacific and Indian Oceans and is part of a wind-driven circulation that is expected to reduce under greenhouse gas forcing. Solar dimming and sulfate aerosol injection geoengineering may reverse this effect. But stratospheric sulfate aerosols affects winds more than simply "shading the sun" and hence reduces the water transport similar as we simulate for unabated greenhouse gas emissions.

Abstract

The Indonesia Throughflow (ITF) is the only low-latitude channel between the Pacific and Indian oceans, and its variability has important effects on global climate and biogeochemical cycles. Climate models consistently predict a decline in ITF transport under global warming, but it has not yet been examined under solar geoengineering scenarios. We use standard parameterized methods for estimating ITF: the Amended Island Rule and Buoyancy Forcing, to investigate ITF under the SSP2-4.5 and SSP5-8.5 greenhouse gas scenarios, and the geoengineering experiments G6solar and G6sulfur that reduce net global mean radiative forcing from SSP5-8.5 levels to SSP2-4.5 levels using solar diming and sulfate aerosol injection strategies. Six model ensemble mean projections for 2080 - 2100 relative to historical

1

(1980-2014) ITF are reductions of 19% under the G6solar scenario and 28% under the G6sulfur scenario which compare with reductions of 23% and 27% under SSP2-4.5 and SSP5-8.5. Despite standard deviations amounting to 5-8% for each scenario, all scenarios are significantly different from each other ($p<0.05$) when taken over the whole 2020-2100 simulation period. Thus, significant weakening of the ITF occurs under all scenarios, but G6solar closer approximates SSP2-4.5 than does G6sulfur. In contrast with the other three scenarios which show only reductions in forcing due to ocean upwelling, the G6sulfur experiment shows a large reduction in ocean surface wind stress forcing accounting for 47% (38% - 65% across model range) of the decline of total ITF transport. There are also reductions in deep-sea upwelling in extratropical western boundary currents.

1. Introduction

The Indonesian Throughflow (ITF) is an important part of the global thermohaline circulation (Gordon, 1986; Lee et al., 2002; Sprintall et al., 2009). The ITF brings about 15 Sv (1 Sv = $10^6 \, m^3/s$; ~10.7 to ~18.7 Sv during the INSTANT Field Program, 2004-2006) of warm and fresh water from the Pacific to the Indian Ocean (Sprintall et al., 2009). Since the ITF is the only ocean pathway in the tropics between the Pacific and Indian Oceans it is the key to heat and water volume transport between them (Godfrey, 1996; Talley, 2008). The ITF also plays an important role in regulating global climate and biogeochemical cycles (Ayers et al., 2014; Hirst and Godfrey, 1994), for example the ITF may influence the El Nino-Southern Oscillation (ENSO) by altering the tropical–subtropical exchange, the structure of the mean tropical thermocline, and the mean sea surface temperature (SST) difference between the Pacific warm Pool and the cold tongue, etc. (Lee et al., 2002) and in the supply of iron in the equatorial upwelling, maintaining biological production in the equatorial eastern Pacific (Gorgues et al., 2007). Sen Gupta et al. (2021) used 26 CMIP6 models to predict ITF weakening by 3 Sv (2.4-3.2 Sv model range) under the SSP5-8.5 scenario (the high greenhouse gas emission scenario) relative to 20th century historical means The decline in the ITF would lead to more heat to accumulate in the Pacific Ocean, which could alter tropical atmospheric-ocean interactions and contribute to extreme El Nino /La Nina events (Cai et al., 2015; Klinger and Garuba, 2016).

57 The ITF is fed by the Mindanao Current and the New Guinea Coast Undercurrent (Figure 1) and, to a

58 lesser extent, parts of the low-latitude Pacific Western Boundary Current (WBC) that flows toward the

59 equator (Godfrey, 1996; Lukas et al., 1996). The ITF helps supply the Agulhas current leakage from the

60 Indian Ocean to the South Atlantic Ocean, and may be said to flush Indian Ocean thermocline waters

61 southward by boosting the Agulhas current (Durgadoo et al., 2017; Gordon, 2005).

62

63 The interannual and decadal variability of the ITF transport is influenced by surface winds in the Pacific

64 and Indian Oceans (Feng et al., 2011; Meyers, 1996). Wyrtki (1987) noticed that the pressure gradient

65 between the Pacific and Indian Oceans dominates the ITF flux, and hence that sea level is a good indicator

66 of upper-ocean ITF transport. The largest volume flux is in July-August and the lowest in January-

67 February.

68

69 Model simulations consistently project that ITF transport will be weakened by increased greenhouse gas

70 (GHG) forcing (Feng et al., 2012; Hu et al., 2015; Sen Gupta et al., 2021; Vecchi and Soden, 2007). The

71 driving force is the weakening of the Pacific trade winds under global warming in the 21st century which

72 then weaken the Mindanao Current, the main inflow route of the ITF (Alory et al., 2007; Duan et al.,

73 2017; Sen Gupta et al., 2012).

74

a) The wind stress integral path and buoyancy region
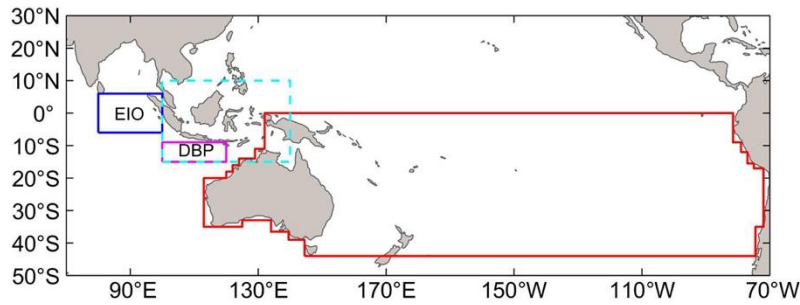
b) Topography of Indonesian Sea
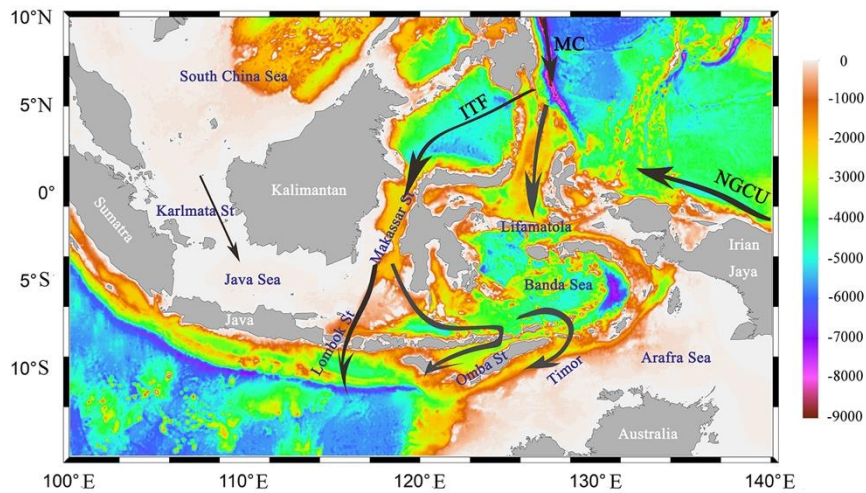
Figure 1. (a) The red line is the wind stress integral path for the Island Rule, The Downstream Buoyant Pool (magenta box) and Equatorial Indian Ocean (blue box) where the density difference is the main index to calculate the ITF transport by buoyance forcing. (b) Inset defined by the cyan dotted line in the panel (a) showing the offshore bathymetry in the maritime continent (ETOPO Global Relief Model, (Amante and Eakins, 2009)) and the Mindanao Current (MC), and the New Guinea Coast Undercurrent (NGCU) paths contributing to the ITF.

Analyzing the water flux through the many shallow channels in the Indonesian archipelago is challenging, and many of these channels are not resolved in simulations with resolutions of a degree or so (Gordon et al., 1999) (Figure 1). This motivates use of alternative methods of estimating ITF. Godfrey (1989) created the Island Rule to estimate flux based on Sverdrup theory (Sverdrup, 1947) analysis of Pacific wind stress. More recently, analysis of climate models revealed the importance of deep ocean circulation to the reduction of ITF transport under GHG forcing. The decline in ITF under GHG forcing could be due

4

89   to both the weakening of trade winds in the Pacific, and deep ocean circulation changes (Feng et al.,

90   2012; Hu et al., 2015). Interannual to decadal, as well as centennial dependence of the ITF on wind and

91   upwelling was found with an eddy-resolving ocean model simulation (Feng et al., 2017). This led to Sen

92   Gupta et al. (2016), and Feng et al. (2017) proposing the Amended Island Rule that modifies the Island

93   Rule to include the estimated net Pacific upwelling contribution to ITF based on high-resolution (1/10°)

94   ocean general circulation modelling.

95

96   An alternative mechanism for the ITF driver was proposed earlier by Andersson and Stigebrandt (2005).

97   In this theory buoyancy forcing is more important than wind forcing in driving the ITF. The ITF

98   variability is found from the baroclinic outflow of the Downstream Buoyant Pool (DBP) that extends

99   over much of the North Australian Basin (Figure 1). Hu and Sprintall (2016) used this method with

100   reanalysis products to produce ITF interannual variability in good agreement with the observed volume

101   transports (2004–2006) from the INSTANT mooring array transport (Sprintall et al., 2009), although the

102   average transport was smaller than the observed transport. INSTANT uses moorings deployed at the

103   major inflow (Makassar Strait, Lifamatola Strait) and outflow passages (Lombok Strait, Ombai Strait

104   and Timor Passage) of the ITF to estimate the ITF transport, resulting in a value of 15 Sv during 2004-

105   2006. While the evidence suggests that the Amended Island Rule explains ITF variability better than

106   buoyancy, changes in buoyancy forcing may affect volume transport of the ITF on decadal scales under

107   a changing climate.

108

109   Solar Radiation Modification (SRM) geoengineering is designed to reduce the solar radiation reaching

110   the surface of the earth and slow down climate warming due to GHG forcing (Shepherd, 2009). Since

111   SRM shortwave forcing has different spatial and temporal variability than longwave forcing, it can only

112   imperfectly offset the climate change caused by the increase of GHGs. In this article we focus on two

113   styles of SRM: reduction of the solar constant to mimic the effect of a sunshade, called solar dimming

114   (SD); and stratospheric aerosol injection (SAI), specifically with injection of sulfate aerosol in the

115   tropical lower stratosphere (Kravitz et al., 2015). These styles of SRM are known to produce over-cooled

116   tropical oceans and under-cooled poles relative to global mean temperatures. However, other styles of

117   injection strategies than the simple tropical site specified by G6 can produce simulated climates without

118   these temperature biases (MacMartin and Kravitz, 2016). Simulated tropical atmospheric circulation

119   systems are impacted under both GHG and solar geoengineering scenarios. Under SD, the seasonal

120   movement of the intertropical convergence zone is reduced relative to GHG climates (Smyth et al., 2017).

121   Both the Hadley and Walker circulations are different from the historical (Cheng et al., 2022; Guo et al.,

122   2018). Impacts of SRM on the Walker circulation are modest compared with the Hadley cell but appear

123   most obviously in relation to the South Pacific Convergence Zone (Guo et al., 2018), which is relevant

124   in the overall tropical Pacific atmosphere system that drives and interacts with the ITF. Greenhouse gas

125   forcing is expected to cause an expansion of the Hadley circulation cells which may be asymmetric

126   between northern and southern hemispheres (Staten et al., 2019). Both SD (Guo et al., 2018) and SAI

127   (Cheng et al., 2022) reduce these greenhouse gas induced changes in the Hadley circulation, although

128   again hemispheric differences remain, and in the Cheng et al. (2022) simulations, were associated with

129   stratospheric heating and tropospheric temperature response due to enhanced stratospheric aerosol

130   concentrations. The changes in stratospheric heating, the tropopause height, and tropical sea surface

131   temperatures may be expected to impact tropical cyclogenesis, and this is consistent with reduction in

132   North Atlantic hurricane numbers and intensity relative to GHG-only climates under SAI (Moore et al.,

133   2015). However, there are differences between tropical basins in expected tropical cyclogenesis potential

134   and significant differences in simulations between climate models (Wang et al., 2018). Potential energy

135   available for extratropical storms is also consistently reduced under SRM relative to GHG

136   forcing(Gertler et al., 2020). The reported impacts highlight the potential role of wind forcing in ITF.

137

138   Little research to date has been done on ocean circulation under SRM, with only the Atlantic Meridional

139   Overturning Circulation (AMOC) having been studied in depth (Hong et al., 2017; Moore et al., 2019;

140   Muri et al., 2018; Tilmes et al., 2020; Xie et al., 2022). Both GHG forcing alone, and with SRM, produce

141   a weakening of AMOC relative to present day, mainly in response to the change of heat flux in the North

142   Atlantic, with little influence from the changes of freshwater flux and wind stress (Hong et al., 2017; Xie

143   et al., 2022). AMOC is less weakened under SRM than with GHG forcing alone and the AMOC declines

144   seen under GHG forcing are consistently reversed by SRM towards present day patterns (Moore et al.,

145   2019; Muri et al., 2018; Tilmes et al., 2020).

146

147   In this study, we will examine the impact of SRM on the change of the ITF in the 21st century, and

148   consider the transport and drivers differences between pure GHG climates representing moderate

149   mitigation (SSP2-4.5) and no mitigation (SSP5-8.5); with solar dimming (G6solar) and stratospheric

150   aerosol injection (G6sulfur) forms of SRM geoengineering.

151

152   **2. Climate Models and Scenarios**

153   The Intergovernmental Panel on Climate Change (IPCC) Shared Socioeconomic Pathways (SSPs) are

154   scenarios defined by radiative forcing goals to be achieved through various climate mitigation policy

155   alternatives (Kriegler et al., 2012; van Vuuren et al., 2011). The climate model simulation results under

156   the SSPs are being performed as part of the Coupled Model Intercomparison Project Phase 6 (CMIP6).

157   We used CMIP6 historical simulation during 1980-2014 (Eyring et al., 2016) and two GHG scenarios

158   during 2015-2100: SSP5-8.5, an unmitigated GHG emission scenario which raises mean global radiative

159   forcing by 8.5 W/m^2 over pre-industrial levels at 2100; and SSP2-4.5 designed to reach peak radiative

160   forcing of 4.5 W/m^2 by mid-century (O'Neill et al., 2016). We use the Geoengineering Model

161   Intercomparison Project Phase 6 (GeoMIP6) G6sulfur and G6solar scenarios during 2020-2100 (Kravitz

162   et al., 2015). The G6sulfur experiment specifies using SAI to reduce the net anthropogenic radiative

163   forcing constantly during the 2020-2100 period from the SSP5-8.5 to the SSP2-4.5 level, while G6solar

164   does the same using SD (Kravitz et al., 2015). The two SRM methods produce significantly different

165   surface climates, with differences from SSP2-4.5 being larger and more spatially variable under G6sulfur

166   than G6solar (Visioni et al., 2021). While the G6 scenarios are not particular realistic, for example they

167   specify starting SAI in 2020 and specify a very simple tropical injection strategy, they do provide a

168   usefully large SRM and GHG signal, and have been simulated by six CMIP6 generation models. This

169   allows more robust findings of the general impacts of SAI, especially when considering aspects of the

170   climate system that have not been addressed to date in geoengineering studies, such as the ITF.

171

172   We used monthly data from the first realization in each scenario from all six Earth System Models (ESM;

Table 1) that have performed the CMIP6 and GeoMIP6 scenarios to estimate the ITF transport. The

variable fields we use are zonal and meridional wind stress (tauu and tauv), sea water vertical velocity

(wo), sea water salinity and temperature (so and thetao) and all fields were interpolated onto a common

$0.5° \times 0.5°$ grid.

Table 1

Earth System Models (ESMs) Used in This Study

Model	Atmospheric Resolution (long × lat)	Ocean Resolution (long × lat)	Reference
CESM2-WACCM	288 × 192	320 × 384	(Danabasoglu et al., 2020)
CNRM-ESM2-1	256 × 128	362 × 294	(Séférian et al., 2019)
IPSL-CM6A-LR	144 × 143	320 × 384	(Boucher et al., 2020)
MPI-ESM1-2-HR	384 × 192	802 × 404	(Mauritsen et al., 2019)
MPI-ESM1-2-LR	192 × 96	256 × 220	(Mauritsen et al., 2019)
UKESM1-0-LL	192 × 144	360 × 330	(Sellar et al., 2019)

3. Methods

3.1 Island Rule

In the Sverdrup balance, ocean current acceleration and friction are neglected, and wind stress curl is the

driving force of large-scale ocean circulation (Sverdrup, 1947). The "Island Rule" (Godfrey, 1989) uses

the Sverdrup balance to calculate the net total flow through a region by the integral of the wind stress on

a specific closed path. This is a simple and more efficient way of estimating the long-term magnitude

and interannual variability than direct observations of flow through the complex channel topography and

equator spanning Indonesian archipelago (Godfrey, 1996). Models have verified that the Island Rule can

capture the decadal variability of the ITF transport (Feng et al., 2011).

The original Island Rule assumes that the ocean is dormant below a moderate depth, *Z,* below which

there is no motion (Sverdrup, 1947). The ITF transport is determined by the integral of wind stress along

the path from the southern tip of Australia, eastwards to South America, following the coastline to the

latitude line of the northwestern tip of Papua New Guinea (PNG) and then traces the west coast of

Australia back to the starting point (Figure 1a):

$$T_{ITF} = \frac{1}{f_N - f_S} \oint \frac{\tau^l}{\rho_0} dl \qquad (1)$$

where, f_N and f_S are the Coriolis parameter at the equator and 44°S, respectively. τ^l is the along route

wind stress component. ρ_0 is the mean sea water density.

3.2 Amended Island Rule

Studies have suggested that a decline in ITF under GHG forcing was due to both the weakening of trade

winds in the Pacific, and the impact of the deep ocean circulation change (Feng et al., 2012; Hu et al.,

2015). Sen Gupta et al. (2016) used a climate model to attribute GHG-forced decrease of the ITF transport

to weakening of deep Pacific upwelling. Feng et al. (2017) estimated the contribution of deep ocean

upwelling from the Pacific north of 44°S to produce the Amended Island Rule:

$$T_{ITF} = \frac{1}{f_N - f_S} \oint \frac{\tau^l}{\rho_0} dl + \iint_{pacific} w_z \, ds \qquad (2)$$

where, w_z is the vertical velocity of the Pacific at 1500 m depth. The Amended Island Rule was verified

with a near-global eddy-resolving ocean model simulation, and found to well-estimate the interannual to

decadal, as well as centennial variabilities of the ITF transport (Feng et al., 2017). Here we describe the

ITF using the Amended Island Rule, and its component parts which are the wind driven Sverdrup balance,

and the Pacific upwelling.

3.3 Buoyancy Forcing

Sea levels in the Pacific and Indian Oceans have been used to estimate the ITF transport in previous

studies (Clarke and Liu, 1994; Potemra et al., 1997; Susanto and Song, 2015). Buoyancy accounts for

high steric sea level (that is a volume increase due to lower density) in the North Pacific (Stigebrandt,

1984). A pool of low-density water (the DBP) originating in the North Pacific is formed in the eastern

Indian Ocean between the Indonesian islands and northwestern Australia (Figure 1a). The sea level drop

between Indian and Pacific Oceans occurs essentially at the abrupt eastern boundary of the DBP and is

the source of buoyancy forcing (Andersson and Stigebrandt, 2005). In the DBP region, the long-term

difference between the westward and eastward transport along the northern and southern flanks of the

222   pool is the ITF transport.

223

224   The geostrophic transport in the DBP is related to denser water in the eastern equatorial Indian Ocean

225   (EIO):

226    $$Q_\lambda = \frac{gH^2\Delta\rho}{2f_\lambda\rho_0} \tag{3}$$

227    $$ITF = Q_{\lambda_N} - Q_{\lambda_S} \tag{4}$$

228   where, g is acceleration due to gravity, H is the penetration depth of the DBP (set by (Andersson and

229   Stigebrandt, 2005) as 1200 m), f_λ is the Coriolis parameter at latitude λ, ρ_0 is the reference density at

230   1200 m, The northern (λ_N) and southern (λ_S) boundary latitudes of the DBP are 10°S and 16°S

231   respectively. $\Delta\rho$ is the density difference between the DBP region (9°S–15°S, 100°E–120°E) and the EIO

232   region (6°N–6°S, 80°E–100°E). Hu and Sprintall (2016) verified the use of DPB and EIO to calculate

233    $\Delta\rho$ with observations.

234

235   **4. Transport and Geoengineering**

236   **4.1 ITF Transport**

237   The multi-model ensemble mean wind driven ITF transport is ~16.9 Sv with the Pacific upwelling north

238   of 44°S contributing ~4.5 Sv in the historical period (Figure 2). This compares with observational

239   estimates of about 15 Sv during 2004-2006 (Sprintall et al., 2009) and the multi-model ensemble (total

240   22 CMIP5 models) mean is 15.2 Sv during 1900-2000 (Sen Gupta et al., 2016). Under SSP2-4.5 during

241   2015 - 2100, the wind-driven and Pacific upwelling contributions to ITF transport are not much different

242   from those under SSP5-8.5. The wind driven volume ITF transport has significant trends for all scenarios

243   with smallest trends for the SSP scenarios (linear trends of lower magnitude than 0.02 Sv per year), while

244   the upwelling contributions has obvious downward trends in all scenarios. These trends appear to be

245   consistent, despite differences in estimated transport across models (Figure S1). Thus the decline in future

246   ITF transport in future GHG climates was explained by (Feng et al., 2017) as due to weakening of the

247   Pacific upwelling on centennial timescales while wind-driven processes had no impact on long

248   timescales.

249

250   During the last 20 years of the 21st century, the simulated ITF transport using the Amended Island Rule

251   is 27% ± 3% (standard error) under SSP5-8.5 (Figure 2c), with Pacific upwelling decline accounting for

252   76%±15% (p<0.05) of the total reduction. Both wind driven and upwelling contributions to ITF transport

253   are slightly higher under SSP2-4.5 than under SSP5-8.5 during the same period, but the differences are

254   small over the whole 2015-2100 period. The total ITF transport is reduced by 23%±2% (standard error,

255   p<0.05) under SSP2-4.5 during the period of 2080-2100 relative to the historical period (13%~27% cross

256   ESM range), and with the wind driven component only dropping by 5% (-2%~9% range). The reductions

257   under SSP5-8.5 for upwelling and wind driven components are respectively 97% (60%~305%) and 8%

258   (1%~19%).

259

260   The multi-mean ITF transport simulated by buoyancy forcing is 7.3 Sv in the historical period, which is

261   less than that by wind driven and only half the transport observed during INSTANT (Sprintall et al.,

262   2009), and there is large across-model variability (Figure S2). Under the two SSPs scenarios, the

263   difference in ITF transport is small with significant trend during 2015-2100. The buoyancy driven

264   estimation method can capture the interannual variability of ITF transport, but it does not perform well

265   on centennial timescales (Hu and Sprintall, 2016), where ITF is much closer that from the wind driven

266   estimation method.

267
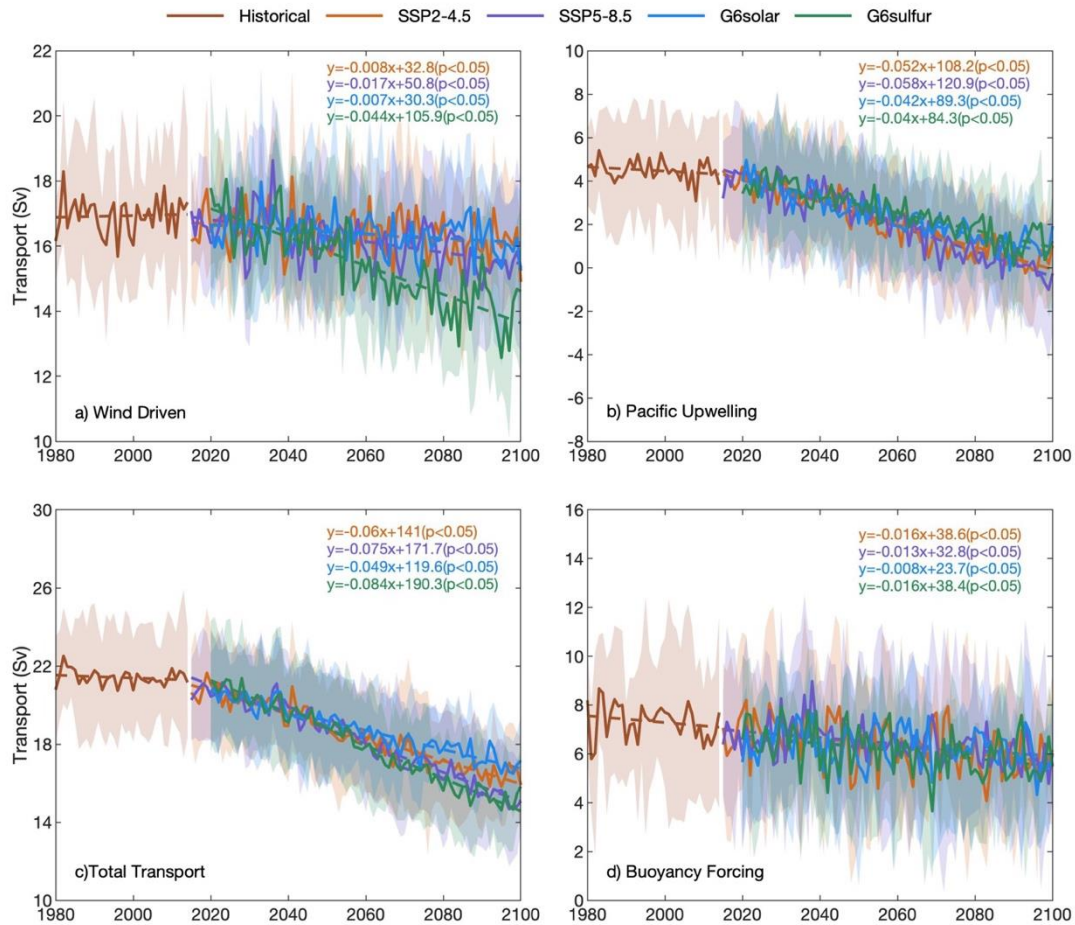
Figure 2. Six ESM ensemble mean ITF components under different scenarios, shadings show the
shadings show the standard deviation and the formula is the trend fitting results under different
scenarios and the significant value (The ranges are 2015-2100 under two SSP scenarios and 2020-2100
under two G6 scenarios), (a) Sverdrup balance wind driven component. (b) Pacific upwelling north of
44°S. (c) Total ITF under the Amended Island Rule (eqn 2). (d) ITF transport by buoyancy forcing.
Individual ESM results are shown in Figure S1.

SAI and SD geoengineering methods clearly have different impacts on wind driven contributions to ITF
transport but smaller although still significant differences in upwelling (Figure 2a,b, Table 2). Under the
G6solar and G6sulfur scenarios, the total ITF transport is reduced by 19%±1% and 28%±1% respectively
during 2080 - 2100 relative to the historical period, of which the wind-driven ITF transport is reduced
by 4%±1% and 16%,±1%, and the upwelling transport volume is reduced by 76%±8% and 70%±10%,

282   all differences are significant (p<0.05), Table 2. Under G6sulfur, the wind driven ITF transport has a

283   clear downward trend in contrast with the other three climate scenarios (Figure 2a). Each ESM also

284   shows consistency in the relative declines under the four future climates (Figure S1a). The decline of

285   wind driven transport accounts for 47% (38% - 65% range) of the decline of total ITF transport under

286   G6sulfur during 2080-2100, and its ensemble mean wind driven transport volume is significantly lower

287   than that under SSP5-8.5 (Table 2). The ensemble mean ITF transport by buoyancy forcing all have

288   significant declining trend under the future climate scenarios but the differences are not generally

289   significant (Figure 2d, Table 2), which is different from the transport change calculated using the wind

290   driven and upwelling contributions.

291

292   The decline in ITF transport via upwelling in future relative to present under all scenarios is illustrated

293   in Figure 3. During the historical period, the zonally integrated upwelling contributions to ITF transport

294   in the Pacific Ocean steadily accumulate when progressing from southern latitudes until about 20°N.

295   Latitudes further north make little contribution and accumulated upwelling is then fairly constant. This

296   pattern changes in all future climate scenario simulations. The Pacific upwelling contributions to

297   transport volume accumulate steadily, but slower with latitude than under the historical simulation, until

298   to just north of the equator (2°N), and then, after a small decrease rapidly accumulates over a few degrees

299   of latitude. North of 20°N, the integrated upwelling declines. Differences in ocean upwelling velocity

300   under different scenarios are not significant in the Pacific, except in the western boundary current region.

301   Starting from 20°N, the wind stress in the western boundary current region decreases, the upwelling of

302   seawater weakens, (Figure 5), resulting in a reduced upwelling contribution in the future scenario.

303   Between 44°S and 15°S, the zonal cumulative transport curves under SSP2-4.5 and G6solar are relatively

304   similar. The integrated upwelling under the G6sulfur scenario transitions from the smallest of the four

305   future scenarios between 44°S and 20°S to the largest a few degrees north of the equator (Figure 3).

306
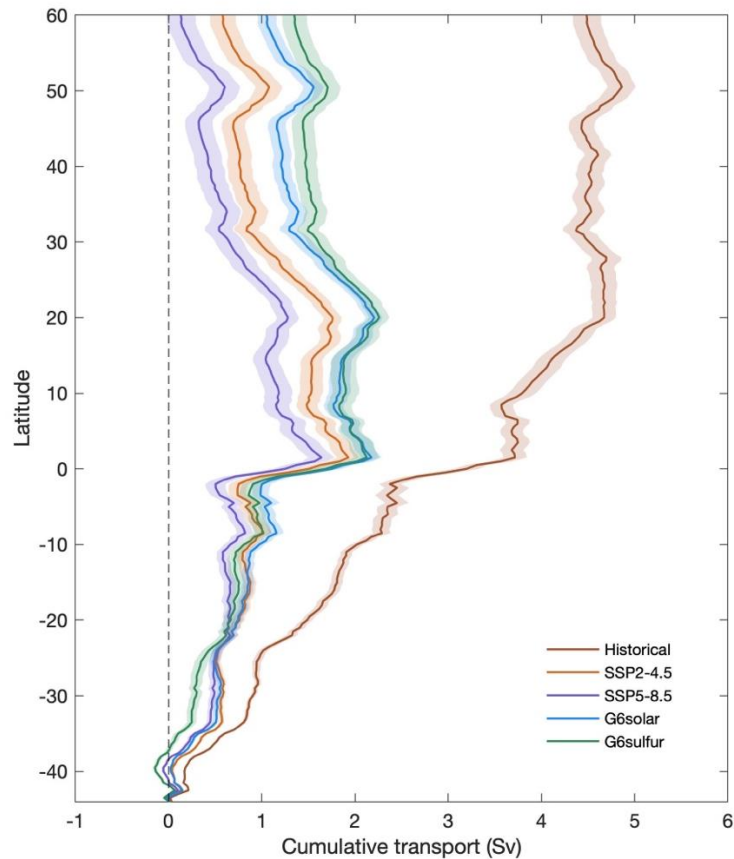
307

308 **Figure3**. Multi-model ensemble mean zonal cumulative transport by Pacific upwelling north of 44°S

309 during the historical simulation (1980-2014) and under the four future scenarios (2080-2100), shadings

310 show the standard error.

311

312 **4.2 ITF by geoengineering type**

313 **4.2.1Wind stress**

314 Godfrey et al. (1993)suggested that the Indonesian throughflow originates in the South Pacific, where

315 the South Equatorial Current retroflects into the North Equatorial Countercurrent and enters the

316 Indonesian Sea via the Mindanao Current. Wind stress curl is determined by the components of the wind

317 stress vector and drives the ocean circulation (Gill and Adrian, 1982). Figure 4a shows the mean wind

318 stress and wind stress curl in the historical period (1980-2014), and the wind stress curl is positive at low

319 latitudes in the South Pacific, causing mass transport to the north. In the South Pacific under the SSP2-

320 4.5 scenario during 2080-2100, the wind stress curl in the middle latitudes is stronger than in the historical

321 period, while that at low latitudes and along the west coast of South America it is weaker than in the

14

322   historical period (Figure 4a). The SSP5-8.5 scenario anomalies relative to the historical period are similar

323   but extend over a larger region and have larger amplitude (Figure 4b). Net ITF transport volume under

324   SSP5-8.5 is lower than the historical, which is consistent with the difference in wind stress curl between

325   the simulations. There is no significant difference in wind stress curl between G6solar and SSP2-4.5 in

326   mid latitudes, and the difference in low latitudes is relatively small (Figure 4c). The wind stress curl

327   under G6solar is slightly weaker at mid latitudes and slightly stronger at low latitude than with SSP5-8.5

328   (Figure 4d). Differences between wind stress curl under G6sulfur and SSP2-4.5 scenarios are mainly in

329   the mid latitudes, near the equator and the west coast of South America (Figure 4e), which are related to

330   the wind driven ITF transport changes. In contrast, the significant differences between the wind stress

331   curl under G6sulfur and SSP5-8.5 are mainly in the northeast of the South Pacific, and the wind stress

332   curl under G6sulfur is stronger than that under SSP5-8.5 (Figure 4f). The wind stress curl at the inlet of

333   the ITF is significantly weakened under the G6sulfur scenario compared with the two SSPs scenarios.

334

335

336

337
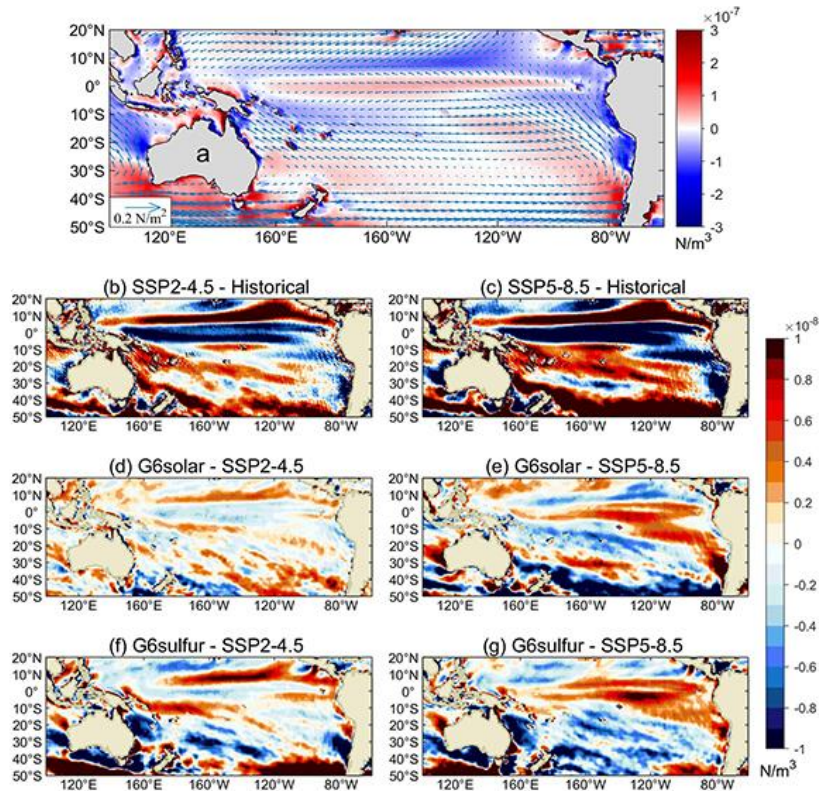
Figure 4. The multi-model mean differences in wind stress curl (a)the historical mean and the arrows show the wind stress, (b) SSP2-4.5 and historical, (c) SSP5-8.5 and historical, (d) G6solar and SSP2-4.5, (e) G6solar and SSP5-8.5, (f) G6sulfur and SSP2-4.5, (g) G6sulfur and SSP5-8.5. The historical period is 1980-2014, and the future scenarios period is 2080-2100. Regions where differences are not significant at the 95% level by the Wilcoxon signed391 rank test are masked in white.

The multi-model average ITF transport between G6 scenarios and SSPs scenarios shows significant differences during 2020-2100 (Table 2). Differences in wind-induced ITF transport from SSP2-4.5 are smallest with G6solar (Table 2) and are not significantly different in every ESM (Table S1). Differences between SSP5-8.5 and G6solar are the same sign for wind and upwelling forcings, contributing to larger differences in the amended island rule total transport. With G6sulfur, differences in wind and upwelling forcing differences from SSP5-8.5 are oppositely signed, and the net transport difference is quite small, but still significant for the six models ensemble. Differences in the ITF defined by buoyancy are only significant for G6sulfur-SSP5-8.5.

16

354

Table 2

The differences in monthly ITF Transport (2020-2100)[a] and its components; Wind is the ITF transport

derived from Island Rule; Upwelling is the area integral of Pacific upwelling rate at 1500m; Total is the

ITF transport calculating by Amended Island Rule; Buoyancy is the ITF transport by buoyancy forcing.

Unit: Sv ($1Sv = 10^6 \, m^3/s$)

360

| Differences	Wind	Upwelling	Total	Buoyancy
G6solar – SSP2-4.5	0.02	**0.33**	**0.35**	-0.06
G6sulfur – SSP2-4.5	**-0.96**	0.53	**-0.44**	-0.21
G6solar – SSP5-8.5	**0.23**	**0.4**	**0.63**	-0.15
G6sulfur – SSP5-8.5	**-0.75**	0.59	**-0.16**	**-0.3**
G6sulfur –G6solar	**-0.98**	0.19	**-0.79**	-0.15

361

[a]The end dates of the G6solar and G6sulfur of MPI-ESM1-2-HR are 2099 and 2089, respectively, and
those of MPI-ESM1-2-LR are both in 2099.   Values in bold are significant at the 95% level according
to the Wilcoxon signed-rank test.

365

4.2.2 Upwelling

The spatial pattern of upwelling velocity at 1500 m in the Pacific under present day conditions is for

strong upwelling at the equator, weak upwelling in the interior, and mixed up- and down-welling along

the ocean boundaries (Feng et al., 2017). In the future climate scenarios, the main factor affecting ITF

transport is net upwelling in the Pacific Ocean(Feng et al., 2017; Sen Gupta et al., 2016). Spatial patterns

of upwelling changes are shown in Figure 5. The western boundary currents are an important source of

ITF gradient differences in wind stress that drive ocean currents (Hu et al., 2015), and these gradients

remain present at great depth in the western boundary current region. Much of the ocean shows no

significant changes in upwelling velocity, but the western boundaries differ significantly from the

historical in both SSP scenarios (Figure 5a,b), and under SSP5-8.5 there is also a significant upwelling

in the equatorial eastern Pacific. The difference of upwelling velocity between G6solar and SSP2-4.5

scenarios is insignificant almost everywhere (Figure 5c), while differences from SSP5-8.5 are significant

mainly along the extratropical western ocean boundaries. G6sulfur differences from the SSP scenarios

are clearly larger than those for G6solar, and are greater in the extratropics than in the tropics. The pattern

380   of changes in upwelling anomalies for G6sulfur-SSP2-4.5 is similar but of opposite sign to G6solar-

381   SSP5-8.5 (Figure 5e), while differences for G6sulfur and SSP5-85 are similar or slightly smaller than

382   differences from SSP2-4.5 (Figure 5f).

383

384
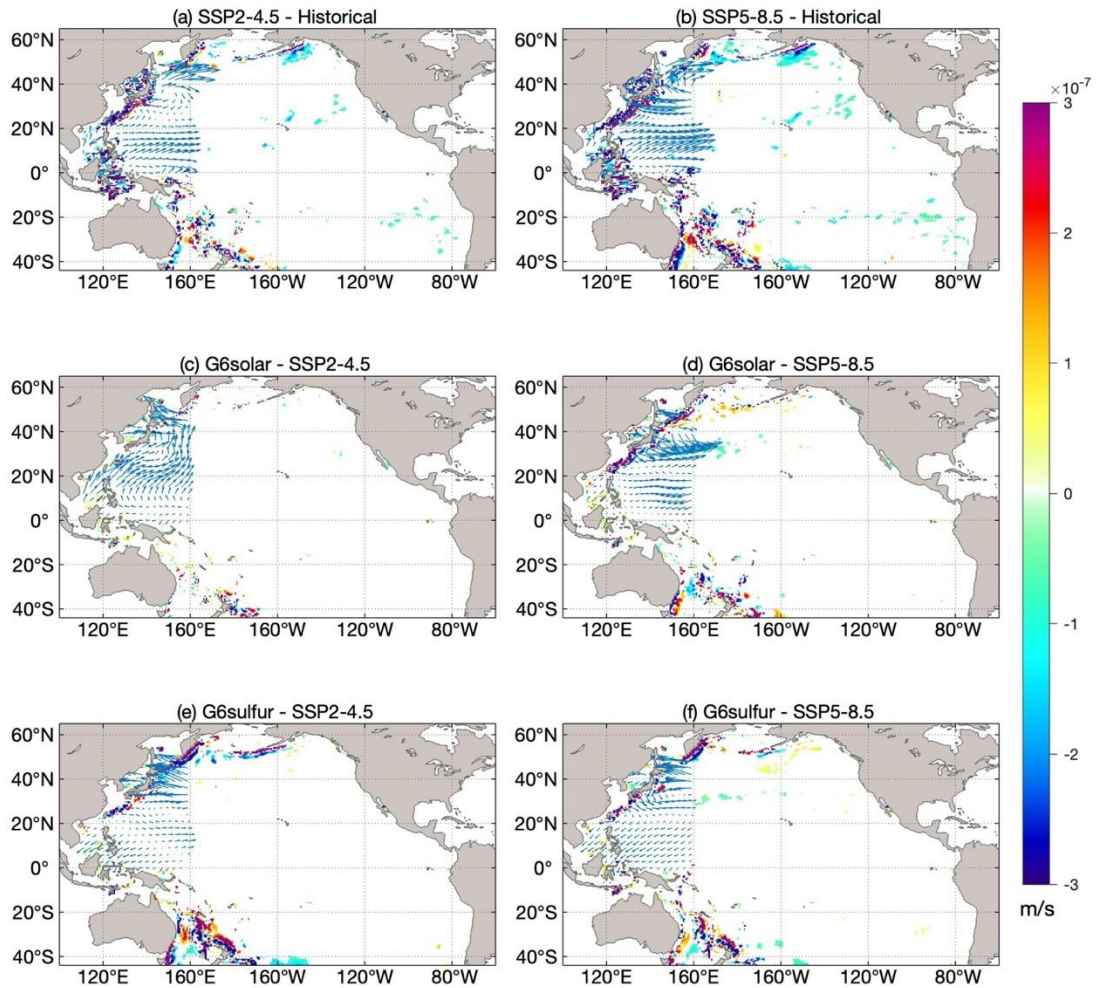
Figure 5. Changes in the multi-model ensemble mean upwelling velocity at 1500m (blue indicates

increased upwelling, red indicates relative downwelling) and wind stress difference (arrow) for (a) SSP2-

4.5 and historical, (b) SSP5-8.5 and historical, (c) G6solar and SSP2-4.5, (d) G6solar and SSP5-8.5, (e)

G6sulfur and SSP2-4.5, (f)G6sulfur and SSP5-8.5. The historical period is 1980-2014, and the future

scenarios period is 2080-2100. Regions where differences are not significant at the 95% level by the

Wilcoxon signed rank test are masked in white.

391

392   **4.2.3 Seasonality**

393   Seasonal patterns in ITF are important and reflect changes in position of the two main precipitation

394   convergence zones across the region. Model simulations show that decreases in ITF transport in April-

395   May and October-November, and their recovery are due to the upper ocean changes associated with the

396   Rossby waves in the Pacific Ocean, and that the seasonal ITF transport is closely related to wind

397   variations in the Pacific and Indian Oceans (Shinoda et al., 2012). The seasonal wind-driven ITF transport

398   is maximum in JJA and minimum in MAM under different scenarios (Figure 6), which is consistent with

399   the result by Wyrtki (1987). However, the differences between the G6 scenarios are largest in DJF and

400   MAM, and these seasons are also when all 4 future scenarios are most different from the historical
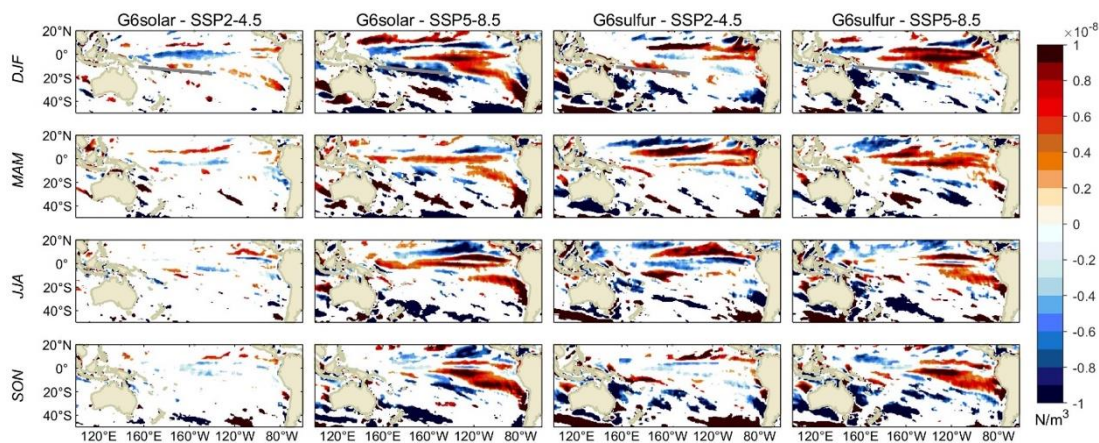
401   simulation.
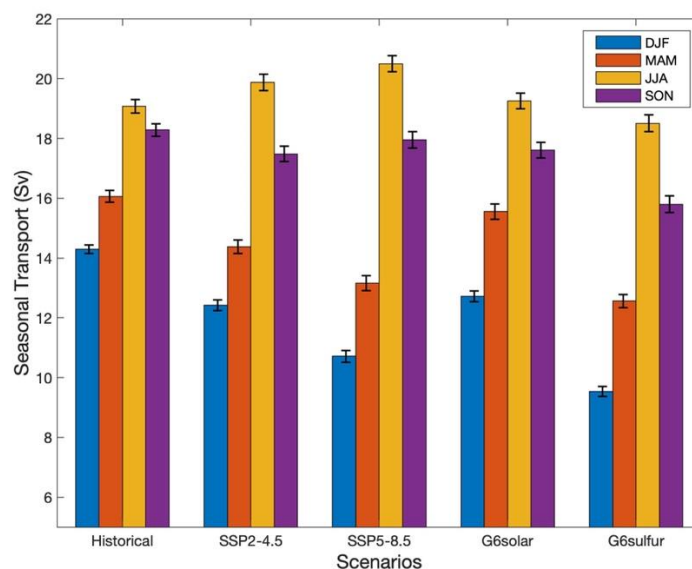
402

403   **Figure 6.** The ensemble mean seasonal wind-driven ITF transport and the standard error under the
404   historical period (1980-2014) and future scenarios (2080-2100).

405

406   The South Pacific Convergence Zone (SPCZ) is a strong rainfall and convection zone extending from

407   the equator to the subtropical South Pacific, which is generated by the low-level convergence between

408   the northeast trade wind and weaker westerly wind (Vincent, 1994). The SPCZ is clearest in December-

409   February (DJF), the Southern hemisphere summer, and is marked in the top row of Figure 7. The annual

410   wind stress curl differences between G6solar and SSP2-4.5 are small, but the seasonal variation

411   difference in some regions is significant. Under G6solar, compared with SSP2-4.5, the wind stress curl

near the equator is weakened in DJF. In March to May (MAM), the wind stress curl in the middle and

low latitudes of the southern hemisphere is generally enhanced. SSP5-8.5 has significantly lower wind

stress curl in the SPCZ region relative to G6solar in DJF. In MAM, their differences are mainly in the

mid latitudes. From June through November (JJA and SON), wind stress curl under SS5-8.5 is significant

lowered between 30 °S and 50 ° S. In contrast G6sulfur shows significant increase in the SPCZ region

in DJF, and a significant decrease the south of SPCZ region in JJA relative to SSP2-4.5. There are large

differences in the ocean northeast of New Zealand with the sign reversing from MAM to JJA. Differences

between G6sulfur and SSP5-8.5 are not very much bigger than from SSP2-4.5, and the patterns are quite

similar. The wind stress curl in the SPCZ region and its extension southeastwards is significantly

weakened under G6sulfur relative to both SSP scenarios in DJF. In JJA the region with decrease in wind

stress curl east from New Zealand is slightly larger relative to SSP5-8.5 and SSP2-4.5.

Figure 7. Seasonal ESM ensemble mean spatial differences (G6solar – SSP2-423 4.5, G6solar – SSP5-8.5, G6sulfur - SSP2-4.5, G6sulfur – SSP5-8.5) of the wind stress curl during 2080-2100. The white lines in each panel of the top row marks the mean the position of the South Pacific Convergence Zone (SPCZ) in DJF based on the CMIP6 multi-model mean (Brown et al., 2020). Regions where differences are not significant at the 95% level by the Wilcoxon signed rank test are masked in white, significant differences are larger than $|0.5\times10^{-8}|$ Nm^{-3}

5. Summary and Discussion

The wind driven ITF transport estimated using the six CMIP6 models historical scenario is well within the range of 11-20 Sv, found from 22 CMIP5 models (Sen Gupta et al., 2016). These model estimates tend to slightly overestimate ITF compared with observed ITF (15±3 Sv) since Godfrey's Island Rule ignores friction due to real ocean topography (Feng et al., 2005; Wajsowicz, 1993). The rather large interannual and decadal variations in the ITF (amounting to several Sv) are mainly influenced by the Pacific and Indian Ocean winds. There is an observed relationship between ITF transport and the El Niño-Southern Oscillation (ENSO), with stronger transport during La Niña and weaker transport during El Niña, with ITF variability lagging ENSO variability by 8-9 months (England and Huang, 2005; Meyers, 1996).

From the wavelet coherence analysis (Grinsted et al., 2004) of Nino3.4 and the wind-driven ITF anomaly, the obvious annual power is easily seen, but is not actually significant against the randomized phase Fourier background hypothesis. There are multi-year significant power in all models, though there are no significant differences in power between the scenarios at any band between annual and decadal. The two appear in anti-phase (Figure 8) in line with observed stronger transport during La Niña and weaker transport during El Niña. At the same time, ITF variability also lags behind ENSO on the whole, but there are differences among different models.

Figure 8. The squared wavelet coherence between the Nino3.4 (representing ENSO) and the wind-driven ITF transport monthly anomalies under the two SSPs (2015-2100) and two G6 (2020-2100) scenarios in six models. The 95% significance level above the background of 1000 Monte-Carlo ensemble of series of identical mean and standard deviation with identical power spectra but phase-randomized Fourier noise (chosen instead of the usual first order autoregressive null hypothesis here because of the strong annual signal; Xia et al. (2023)), is represented by a thick contour line. The arrows indicate the relative phase relationship, that is, in-phase points to the right, anti-phase points to the left, the arrow up indicates that the ITF anomaly leads ENSO by 90°, and a down arrow indicates that the ITF anomaly lags ENSO by 90°.

The six ESM we use concur on weakening of ITF transport in all future scenarios. That is SRM cannot restore the ITF to its historic levels (Table 2, Fig 2). This contrasts somewhat to the changes simulated in the AMOC under SRM with GHG forcing, where it seems that SRM can partly reverse the slow down in AMOC induced by GHG forcing, reducing impacts from around 35% to 24% (Muri et al., 2018; Tilmes et al., 2020; Xie et al., 2022). This illustrates the important regional variability in responses to SRM.

Weakening of the ITF transport appears in all future scenarios, both with pure GHG forcing, and

22

469 combining GHG and SRM strategies. The ITF transport changes are defined almost totally (around 90%)

470 by significant differences in Pacific upwelling (Figure 2a and 2b). This is consistent with the conclusion

471 that the weakening trend of ITF under global warming predicted by high-precision ocean models is not

472 directly related to the change of Pacific trade winds but to the reduction of Pacific deep-sea upwelling

473 (Feng et al., 2017). On centennial scales, the decrease of the net deep ocean upwelling in the tropics and

474 the South Pacific, especially the changes in the western boundary current system is what determines ITF

475 transport. Buoyancy forcing can only estimate the interannual variation of the ITF, and our study

476 supports the utility of the Amened Island Rule in estimating centennial changes in ITF transport.

477

478 Sen Gupta et al. (2021) note that projected weakening of the ITF and differences between ESM can be

479 explained by changes in large-scale surface winds. This contrasts with our findings where changes in

480 wind driven transport are not significantly different between models, but instead upwelling in the

481 extratropical western boundary zones dominates changes between scenarios. However, western boundary

482 currents are deep and narrow and differ from the shallow and wide eastern boundary currents. The tropics

483 experience weaker (and reversed) trade winds from those that dominate the extratropical regions. The

484 geographical differences in upwelling suggest that wind changes are driving the overall changes in ITF

485 via upwelling regions, and so in effect supporting the conclusion of Sen Gupta et al. (2021) that

486 differences in future surface winds explain most of the differences in future large scale current systems.

487

488 SSP2-4.5 global radiative forcing was the design target of the G6 experiments despite GHG

489 concentrations being at SSP5-8.5 levels. The difference in wind stress curl between G6solar and SSP2-

490 4.5 indicates that the SD experiment performs better at reversing GHG induced changes in Pacific wind

491 than G6sulfur. The G6sulfur SAI experiment leads to a significant change in the winds in mid and low

492 latitude Pacific Ocean, which results in even lower estimated ITF transport than under the high GHG

493 SSP5-8.5 forcing alone. Furthermore, G6sulfur also impacts deep ocean upwelling especially in the

494 extratropical western boundary current region, such that the ITF transport during the 21st century under

495 the G6sulfur scenario is slower than that under the G6solar scenario. The G6 scenarios do not affect low

496 latitude western boundary currents and upwelling, for example the upwelling near the Mindanao current

497 is unaffected while the upwelling along the Kuroshio current is apparently displaced in both G6

498 experiments. The ITF transport under the SD experiment was stronger than under the SAI experiment

499 and even higher than its target SSP2-4.5 scenario level at the end of the 21st century.

500

501 Changes in circulation in the future will have important impacts on aquatic ecology and fisheries (Dubois

502 et al., 2016). In fact, the population in Indonesia's coastal areas, especially those in the islands through

503 which the ITF passes, are highly dependent on fisheries and hence, the changes in ITF under both pure

504 GHG and mixed GHG and SRM scenarios will have important local implications on the livelihood and

505 ways of life of the local populations. Seasonal variations in ITF transport reflect important processes in

506 the tropical convergence zones, and these are clearly impacted by all 4 future scenarios in generally subtle

507 ways. But the largest differences are seen between the two most challenging scenarios to simulate –

508 SSP5-8.5 and G6sulfur. Despite the large size of perturbation that these forcings apply in the simulations,

509 and the differences between climate models in parameterizing the SAI schemes, the finding are rather

510 robust in the changes of winds in all seasons in the Pacific Ocean and Maritime Continent.

511

512 SAI is a far more feasible method of SRM than SD (Shepherd, 2009), but it produces far larger

513 differences in various climate fields from GHG and historic simulations than does SD (Visioni et al.,

514 2021), and far larger across-ESM differences as the models process the aerosol impacts in varied ways

515 (Visioni et al., 2021). The differences in winds noted in G6sulfur likely arise from differences in

516 stratospheric heating due to the sulfur aerosols that then drive tropospheric circulation changes (Visioni

517 et al., 2020).

518

519 Although ESM can provide reliable predictions of the ITF transport, the accuracy of global meso- and

520 small-scale spatial and seasonal changes remains an issue. These relatively small-scale differences are

521 potentially more important for local impacts than differences in larger scale or annual changes. These

522 aspects will need to be explored using impact models tailored to the region, ideally through initiatives

523 focused on the Global South like the Degrees Initiative (https://www.degrees.ngo/) and addressing

524 concerns raised by local rightsholders.

525

Code and data availability

All model data used in this work are available from the Earth System Grid Federation (WCRP, 2022;

https://esgf-node.llnl.gov/projects/cmip6, last access: 3 July 2022).

Author contributions

JCM conceived and designed the analysis. CS collected the data and performed the analysis. CS and

JCM wrote the paper. All authors contributed to the discussion.

Competing interests

The contact author has declared that neither they nor their co-authors have any competing interests.

538

Reference

Alory, G., Wijffels, S., and Meyers, G.: Observed temperature trends in the Indian Ocean over 1960–
1999 and associated mechanisms, Geophys. Res. Lett., 34,
https://doi.org/10.1029/2006gl028044, 2007.

Amante, C., and Eakins, B. W.: ETOPO1 arc-minute global relief model: procedures, data sources and
analysis, NOAA Tech. Memo. NESDIS NGDC-24, https://doi.org/10.7289/V5C8276M, 2009.

Andersson, H. C., and Stigebrandt, A.: Regulation of the Indonesian throughflow by baroclinic draining
of the North Australian Basin, Deep Sea Res., Part I, 52, 2214-2233,
https://doi.org/10.1016/j.dsr.2005.06.014, 2005.

Ayers, J. M., Strutton, P. G., Coles, V. J., Hood, R. R., and Matear, R. J.: Indonesian throughflow nutrient
fluxes and their potential impact on Indian Ocean productivity, Geophys. Res. Lett., 41, 5060-
5067, https://doi.org/10.1002/2014gl060593, 2014.

Boucher, O., Servonnat, J., Albright, A. L., Aumont, O., Balkanski, Y., Bastrikov, V., Bekki, S., Bonnet,
R., Bony, S., Bopp, L., Braconnot, P., Brockmann, P., Cadule, P., Caubel, A., Cheruy, F., Codron,
F., Cozic, A., Cugnet, D., D'Andrea, F., Davini, P., Lavergne, C., Denvil, S., Deshayes, J.,
Devilliers, M., Ducharne, A., Dufresne, J. L., Dupont, E., Éthé, C., Fairhead, L., Falletti, L.,
Flavoni, S., Foujols, M. A., Gardoll, S., Gastineau, G., Ghattas, J., Grandpeix, J. Y., Guenet, B.,
Guez, L. E., Guilyardi, E., Guimberteau, M., Hauglustaine, D., Hourdin, F., Idelkadi, A.,
Joussaume, S., Kageyama, M., Khodri, M., Krinner, G., Lebas, N., Levavasseur, G., Lévy, C.,
Li, L., Lott, F., Lurton, T., Luyssaert, S., Madec, G., Madeleine, J. B., Maignan, F., Marchand,
M., Marti, O., Mellul, L., Meurdesoif, Y., Mignot, J., Musat, I., Ottlé, C., Peylin, P., Planton, Y.,

Polcher, J., Rio, C., Rochetin, N., Rousset, C., Sepulchre, P., Sima, A., Swingedouw, D., Thié blemont, R., Traore, A. K., Vancoppenolle, M., Vial, J., Vialard, J., Viovy, N., and Vuichard, N.: Presentation and Evaluation of the IPSL‐CM6A‐LR Climate Model, J. Adv. Model. Earth Syst., 12, https://doi.org/10.1029/2019ms002010, 2020.

Cai, W., Santoso, A., Wang, G., Yeh, S.-W., An, S.-I., Cobb, K. M., Collins, M., Guilyardi, E., Jin, F.-F., Kug, J.-S., Lengaigne, M., McPhaden, M. J., Takahashi, K., Timmermann, A., Vecchi, G., Watanabe, M., and Wu, L.: ENSO and greenhouse warming, Nat. Clim. Change, 5, 849-859, https://doi.org/10.1038/nclimate2743, 2015.

Cheng, W., MacMartin, D. G., Kravitz, B., Visioni, D., Bednarz, E. M., Xu, Y., Luo, Y., Huang, L., Hu, Y., Staten, P. W., Hitchcock, P., Moore, J. C., Guo, A., and Deng, X.: Changes in Hadley circulation and intertropical convergence zone under strategic stratospheric aerosol geoengineering, npj Clim. Atmos. Sci., 5, https://doi.org/10.1038/s41612-022-00254-6, 2022.

Clarke, A. J., and Liu, X.: Interannual sea level in the northern and eastern Indian Ocean, J. Phys. Oceanogr., 24, 1224-1235, https://doi.org/10.1175/1520-0485(1994)024<1224:ISLITN>2.0.CO;2, 1994.

Danabasoglu, G., Lamarque, J. F., Bacmeister, J., Bailey, D. A., DuVivier, A. K., Edwards, J., Emmons, L. K., Fasullo, J., Garcia, R., Gettelman, A., Hannay, C., Holland, M. M., Large, W. G., Lauritzen, P. H., Lawrence, D. M., Lenaerts, J. T. M., Lindsay, K., Lipscomb, W. H., Mills, M. J., Neale, R., Oleson, K. W., Otto‐Bliesner, B., Phillips, A. S., Sacks, W., Tilmes, S., Kampenhout, L., Vertenstein, M., Bertini, A., Dennis, J., Deser, C., Fischer, C., Fox‐Kemper, B., Kay, J. E., Kinnison, D., Kushner, P. J., Larson, V. E., Long, M. C., Mickelson, S., Moore, J. K., Nienhouse, E., Polvani, L., Rasch, P. J., and Strand, W. G.: The Community Earth System Model Version 2 (CESM2), J. Adv. Model. Earth Syst., 12, https://doi.org/10.1029/2019ms001916, 2020.

Duan, J., Chen, Z., and Wu, L.: Projected changes of the low-latitude north-western Pacific wind-driven circulation under global warming, Geophys. Res. Lett., 44, 4976-4984, https://doi.org/10.1002/2017gl073355, 2017.

Dubois, M., Rossi, V., Ser-Giacomi, E., Arnaud-Haond, S., López, C., and Hernández-García, E.: Linking basin-scale connectivity, oceanography and population dynamics for the conservation and management of marine ecosystems, Global Ecol. Biogeogr., 25, 503-515, https://doi.org/10.1111/geb.12431, 2016.

Durgadoo, J. V., Rühs, S., Biastoch, A., and Böning, C. W. B.: Indian Ocean sources of Agulhas leakage, J. Geophys. Res.: Oceans, 122, 3481-3499, https://doi.org/10.1002/2016jc012676, 2017.

England, M. H., and Huang, F.: On the interannual variability of the Indonesian Throughflow and its linkage with ENSO, J. Clim., 18, 1435-1444, https://doi.org/10.1175/JCLI3322.1, 2005.

Eyring, V., Bony, S., Meehl, G. A., Senior, C. A., Stevens, B., Stouffer, R. J., and Taylor, K. E.: Overview of the Coupled Model Intercomparison Project Phase 6 (CMIP6) experimental design and organization, Geosci. Model Dev., 9, 1937-1958, https://doi.org/10.5194/gmd-9-1937-2016, 2016.

Feng, M., Böning, C., Biastoch, A., Behrens, E., Weller, E., and Masumoto, Y.: The reversal of the multi-decadal trends of the equatorial Pacific easterly winds, and the Indonesian Throughflow and Leeuwin Current transports, Geophys. Res. Lett., 38, L11604,

602   https://doi.org/10.1029/2011gl047291, 2011.

603   Feng, M., Sun, C., Matear, R. J., Chamberlain, M. A., Craig, P., Ridgway, K. R., and Schiller, A.: Marine
604   Downscaling of a Future Climate Scenario for Australian Boundary Currents, J. Clim., 25, 2947-
605   2962, https://doi.org/10.1175/jcli-d-11-00159.1, 2012.

606   Feng, M., Wijffels, S., Godfrey, S., and Meyers, G.: Do eddies play a role in the momentum balance of
607   the Leeuwin Current?, J. Phys. Oceanogr., 35, 964-975, https://doi.org/10.1175/JPO2730.1,
608   2005.

609   Feng, M., Zhang, X., Sloyan, B., and Chamberlain, M.: Contribution of the deep ocean to the centennial
610   changes of the Indonesian Throughflow, Geophys. Res. Lett., 44, 2859-2867,
611   https://doi.org/10.1002/2017gl072577, 2017.

612   Gertler, C. G., O'Gorman, P. A., Kravitz, B., Moore, J. C., Phipps, S. J., and Watanabe, S.: Weakening of
613   the Extratropical Storm Tracks in Solar Geoengineering Scenarios, Geophys. Res. Lett., 47,
614   https://doi.org/10.1029/2020gl087348, 2020.

615   Gill, A. E., and Adrian, E.: Atmosphere-ocean dynamics: Academic press,30 pp., ISBN0122835220,
616   1982.

617   Grinsted, A. J. C. Moore, S. Jevrejeva Application of the cross wavelet transform and wavelet coherence
618   to geophysical time series, Nonlinear Processes in Geophysics, 11, 561-566 2004

619   Godfrey, J., Wilkin, J., and Hirst, A.: Why does the Indonesian Throughflow appear to originate from the
620   North Pacific?, J. Phys. Oceanogr., 23, 1087-1098, https://doi.org/10.1175/1520-
621   0485(1993)023%3C1087:WDTITA%3E2.0.CO;2, 1993.

622   Godfrey, J. S.: A sverdrup model of the depth-integrated flow for the world ocean allowing for island
623   circulations, Geophys. Astrophys. Fluid Dyn., 45, 89-112,
624   https://doi.org/10.1080/03091928908208894, 1989.

625   Godfrey, J. S.: The effect of the Indonesian throughflow on ocean circulation and heat exchange with the
626   atmosphere: A review, J. Geophys. Res.: Oceans, 101, 12217-12237,
627   https://doi.org/10.1029/95jc03860, 1996.

628   Gordon, A. L.: Interocean exchange of thermocline water, J. Geophys. Res.: Oceans, 91, 5037-5046,
629   https://doi.org/10.1029/JC091iC04p05037, 1986.

630   Gordon, A. L.: The Indonesian Seas, Oceanogr., 18, 14, https://doi.org/10.5670/oceanog.2005.01, 2005.

631   Gordon, A. L., Susanto, R. D., and Ffield, A.: Throughflow within Makassar Strait, Geophys. Res. Lett.,
632   26, 3325-3328, https://doi.org/10.1029/1999GL002340, 1999.

633   Gorgues, T., Menkes, C., Aumont, O., Dandonneau, Y., Madec, G., and Rodgers, K.: Indonesian
634   throughflow control of the eastern equatorial Pacific biogeochemistry, Geophys. Res. Lett., 34,
635   https://doi.org/10.1029/2006gl028210, 2007.

636   Guo, A., Moore, J. C., and Ji, D.: Tropical atmospheric circulation response to the G1 sunshade
637   geoengineering radiative forcing experiment, Atmos. Chem. Phys., 18, 8689-8706,
638   https://doi.org/10.5194/acp-18-8689-2018, 2018.

639   Hirst, A. C., and Godfrey, J.: The response to a sudden change in Indonesian throughflow in a global
640   ocean GCM, J. Phys. Oceanogr., 24, 1895-1910, https://doi.org/10.1175/1520-
641   0485(1994)024<1895:TRTASC>2.0.CO;2, 1994.

642   Hong, Y., Moore, J. C., Jevrejeva, S., Ji, D., Phipps, S. J., Lenton, A., Tilmes, S., Watanabe, S., and Zhao,
643   L.: Impact of the GeoMIP G1 sunshade geoengineering experiment on the Atlantic meridional

overturning circulation, Environ. Res. Lett., 12, https://doi.org/10.1088/1748-9326/aa5fb8, 2017.

Hu, D., Wu, L., Cai, W., Gupta, A. S., Ganachaud, A., Qiu, B., Gordon, A. L., Lin, X., Chen, Z., Hu, S., Wang, G., Wang, Q., Sprintall, J., Qu, T., Kashino, Y., Wang, F., and Kessler, W. S.: Pacific western boundary currents and their roles in climate, Nat., 522, 299-308, https://doi.org/10.1038/nature14504, 2015.

Hu, S., and Sprintall, J.: Interannual variability of the Indonesian Throughflow: The salinity effect, J. Geophys. Res.: Oceans, 121, 2596-2615, https://doi.org/10.1002/2015jc011495, 2016.

Klinger, B. A., and Garuba, O. A.: Ocean Heat Uptake and Interbasin Transport of the Passive and Redistributive Components of Surface Heating, J. Clim., 29, 7507-7527, https://doi.org/10.1175/JCLI-D-16-0138.1, 2016.

Kravitz, B., Robock, A., Tilmes, S., Boucher, O., English, J. M., Irvine, P. J., Jones, A., Lawrence, M. G., MacCracken, M., Muri, H., Moore, J. C., Niemeier, U., Phipps, S. J., Sillmann, J., Storelvmo, T., Wang, H., and Watanabe, S.: The Geoengineering Model Intercomparison Project Phase 6 (GeoMIP6): simulation design and preliminary results, Geosci. Model Dev., 8, 3379-3392, https://doi.org/10.5194/gmd-8-3379-2015, 2015.

Kriegler, E., O'Neill, B. C., Hallegatte, S., Kram, T., Lempert, R. J., Moss, R. H., and Wilbanks, T.: The need for and use of socio-economic scenarios for climate change analysis: A new approach based on shared socio-economic pathways, Global Environ. Change, 22, 807-822, https://doi.org/10.1016/j.gloenvcha.2012.05.005, 2012.

Lee, T., Fukumori, I., Menemenlis, D., Xing, Z., and Fu, L.-L.: Effects of the Indonesian throughflow on the Pacific and Indian Oceans, J. Phys. Oceanogr., 32, 1404-1429, https://doi.org/10.1175/1520-0485(2002)032<1404:EOTITO>2.0.CO;2, 2002.

Lukas, R., Yamagata, T., and McCreary, J. P.: Pacific low-latitude western boundary currents and the Indonesian throughflow, J. Geophys. Res.: Oceans, 101, 12209-12216, https://doi.org/10.1029/96jc01204, 1996.

MacMartin, D. G., and Kravitz, B.: Dynamic climate emulators for solar geoengineering, Atmos. Chem. Phys., 16, 15789-15799, https://doi.org/10.5194/acp-16-15789-2016, 2016.

Mauritsen, T., Bader, J., Becker, T., Behrens, J., Bittner, M., Brokopf, R., Brovkin, V., Claussen, M., Crueger, T., Esch, M., Fast, I., Fiedler, S., Flaschner, D., Gayler, V., Giorgetta, M., Goll, D. S., Haak, H., Hagemann, S., Hedemann, C., Hohenegger, C., Ilyina, T., Jahns, T., Jimenez-de-la-Cuesta, D., Jungclaus, J., Kleinen, T., Kloster, S., Kracher, D., Kinne, S., Kleberg, D., Lasslop, G., Kornblueh, L., Marotzke, J., Matei, D., Meraner, K., Mikolajewicz, U., Modali, K., Mobis, B., Muller, W. A., Nabel, J., Nam, C. C. W., Notz, D., Nyawira, S. S., Paulsen, H., Peters, K., Pincus, R., Pohlmann, H., Pongratz, J., Popp, M., Raddatz, T. J., Rast, S., Redler, R., Reick, C. H., Rohrschneider, T., Schemann, V., Schmidt, H., Schnur, R., Schulzweida, U., Six, K. D., Stein, L., Stemmler, I., Stevens, B., von Storch, J. S., Tian, F., Voigt, A., Vrese, P., Wieners, K. H., Wilkenskjeld, S., Winkler, A., and Roeckner, E.: Developments in the MPI-M Earth System Model version 1.2 (MPI-ESM1.2) and Its Response to Increasing CO2, J. Adv. Model. Earth Syst., 11, 998-1038, https://doi.org/10.1029/2018MS001400, 2019.

Meyers, G.: Variation of Indonesian throughflow and the El Niño-southern oscillation, J. Geophys. Res.: Oceans, 101, 12255-12263, https://doi.org/10.1029/95JC03729, 1996.

Moore, J. C., Grinsted, A., Guo, X., Yu, X., Jevrejeva, S., Rinke, A., Cui, X., Kravitz, B., Lenton, A., Watanabe, S., and Ji, D.: Atlantic hurricane surge response to geoengineering, Proc. Natl. Acad. Sci. U. S. A., 112, 13794-13799, https://doi.org/10.1073/pnas.1510530112, 2015.

Moore, J. C., Yue, C., Zhao, L., Guo, X., Watanabe, S., and Ji, D.: Greenland Ice Sheet Response to Stratospheric Aerosol Injection Geoengineering, Earth. Fut., 7, 1451-1463, https://doi.org/10.1029/2019EF001393, 2019.

Muri, H., Tjiputra, J., Otterå, O. H., Adakudlu, M., Lauvset, S. K., Grini, A., Schulz, M., Niemeier, U., and Kristjánsson, J. E.: Climate Response to Aerosol Geoengineering: A Multimethod Comparison, J. Clim., 31, 6319-6340, https://doi.org/10.1175/jcli-d-17-0620.1, 2018.

O'Neill, B. C., Tebaldi, C., Vuuren, D. P. v., Eyring, V., Friedlingstein, P., Hurtt, G., Knutti, R., Kriegler, E., Lamarque, J.-F., and Lowe, J.: The scenario model intercomparison project (ScenarioMIP) for CMIP6, Geosci. Model Dev., 9, 3461-3482, https://doi.org/10.5194/gmd-9-3461-2016, 2016.

Potemra, J. T., Lukas, R., and Mitchum, G. T.: Large-scale estimation of transport from the Pacific to the Indian Ocean, J. Geophys. Res.: Oceans, 102, 27795-27812, https://doi.org/10.1029/97jc01719, 1997.

Séférian, R., Nabat, P., Michou, M., Saint-Martin, D., Voldoire, A., Colin, J., Decharme, B., Delire, C., Berthet, S., Chevallier, M., Sénési, S., Franchisteguy, L., Vial, J., Mallet, M., Joetzjer, E., Geoffroy, O., Guérémy, J. F., Moine, M. P., Msadek, R., Ribes, A., Rocher, M., Roehrig, R., Salas-y-Mélia, D., Sanchez, E., Terray, L., Valcke, S., Waldman, R., Aumont, O., Bopp, L., Deshayes, J., Éthé, C., and Madec, G.: Evaluation of CNRM Earth System Model, CNRM-ESM2-1: Role of Earth System Processes in Present-Day and Future Climate, J. Adv. Model. Earth Syst., 11, 4182-4227, https://doi.org/10.1029/2019ms001791, 2019.

Sellar, A. A., Jones, C. G., Mulcahy, J. P., Tang, Y., Yool, A., Wiltshire, A., O'Connor, F. M., Stringer, M., Hill, R., Palmieri, J., Woodward, S., Mora, L., Kuhlbrodt, T., Rumbold, S. T., Kelley, D. I., Ellis, R., Johnson, C. E., Walton, J., Abraham, N. L., Andrews, M. B., Andrews, T., Archibald, A. T., Berthou, S., Burke, E., Blockley, E., Carslaw, K., Dalvi, M., Edwards, J., Folberth, G. A., Gedney, N., Griffiths, P. T., Harper, A. B., Hendry, M. A., Hewitt, A. J., Johnson, B., Jones, A., Jones, C. D., Keeble, J., Liddicoat, S., Morgenstern, O., Parker, R. J., Predoi, V., Robertson, E., Siahaan, A., Smith, R. S., Swaminathan, R., Woodhouse, M. T., Zeng, G., and Zerroukat, M.: UKESM1: Description and Evaluation of the U.K. Earth System Model, J. Adv. Model. Earth Syst., 11, 4513-4558, https://doi.org/10.1029/2019ms001739, 2019.

Sen Gupta, A., Ganachaud, A., McGregor, S., Brown, J. N., and Muir, L.: Drivers of the projected changes to the Pacific Ocean equatorial circulation, Geophys. Res. Lett., 39, L09605, https://doi.org/10.1029/2012gl051447, 2012.

Sen Gupta, A., McGregor, S., Sebille, E., Ganachaud, A., Brown, J. N., and Santoso, A.: Future changes to the Indonesian Throughflow and Pacific circulation: The differing role of wind and deep circulation changes, Geophys. Res. Lett., 43, 1669-1678, https://doi.org/10.1002/2016gl067757, 2016.

Sen Gupta, A., Stellema, A., Pontes, G. M., Taschetto, A. S., Verges, A., and Rossi, V.: Future changes to the upper ocean Western Boundary Currents across two generations of climate models, Sci. Rep., 11, 9538, https://doi.org/10.1038/s41598-021-88934-w, 2021.

Shepherd, J. G.: Geoengineering the climate: science, governance and uncertainty: Royal Society,

728   London,98 pp., ISBN085403773X, 2009.

729   Shinoda, T., Han, W., Metzger, E. J., and Hurlburt, H. E.: Seasonal Variation of the Indonesian
730   Throughflow in Makassar Strait, J. Phys. Oceanogr., 42, 1099-1123,
731   https://doi.org/10.1175/jpo-d-11-0120.1, 2012.

732   Smyth, J. E., Russotto, R. D., and Storelvmo, T.: Thermodynamic and dynamic responses of the
733   hydrological cycle to solar dimming, Atmos. Chem. Phys., 17, 6439-6453,
734   https://doi.org/10.5194/acp-17-6439-2017, 2017.

735   Sprintall, J., Wijffels, S. E., Molcard, R., and Jaya, I.: Direct estimates of the Indonesian Throughflow
736   entering the Indian Ocean: 2004–2006, J. Geophys. Res., 114,
737   https://doi.org/10.1029/2008jc005257, 2009.

738   Staten, P. W., Grise, K. M., Davis, S. M., Karnauskas, K., and Davis, N.: Regional Widening of Tropical
739   Overturning: Forced Change, Natural Variability, and Recent Trends, J. Geophys. Res.: Atmos.,
740   124, 6104-6119, https://doi.org/10.1029/2018JD030100, 2019.

741   Stigebrandt, A.: The North Pacific: A global-scale estuary, J. Phys. Oceanogr., 14, 464-470,
742   https://doi.org/10.1175/1520-0485(1984)014<0464:TNPAGS>2.0.CO;2, 1984.

743   Susanto, R. D., and Song, Y. T.: Indonesian throughflow proxy from satellite altimeters and gravimeters,
744   J. Geophys. Res.: Oceans, 120, 2844-2855, https://doi.org/10.1002/2014jc010382, 2015.

745   Sverdrup, H. U.: Wind-driven currents in a baroclinic ocean; with application to the equatorial currents
746   of the eastern Pacific, Proc. Natl. Acad. Sci. U. S. A., 33, 318,
747   https://doi.org/10.1073/pnas.33.11.318, 1947.

748   Talley, L. D.: Freshwater transport estimates and the global overturning circulation: Shallow, deep and
749   throughflow components, Prog. Oceanogr., 78, 257-303,
750   https://doi.org/10.1016/j.pocean.2008.05.001, 2008.

751   Tilmes, S., MacMartin, D. G., Lenaerts, J. T. M., van Kampenhout, L., Muntjewerf, L., Xia, L., Harrison,
752   C. S., Krumhardt, K. M., Mills, M. J., Kravitz, B., and Robock, A.: Reaching 1.5 and 2.0 °C
753   global surface temperature targets using stratospheric aerosol geoengineering, Earth Syst.
754   Dynam., 11, 579-601, https://doi.org/10.5194/esd-11-579-2020, 2020.

755   van Vuuren, D. P., Edmonds, J., Kainuma, M., Riahi, K., Thomson, A., Hibbard, K., Hurtt, G. C., Kram,
756   T., Krey, V., Lamarque, J.-F., Masui, T., Meinshausen, M., Nakicenovic, N., Smith, S. J., and
757   Rose, S. K.: The representative concentration pathways: an overview, Clim. Change, 109, 5-31,
758   https://doi.org/10.1007/s10584-011-0148-z, 2011.

759   Vecchi, G. A., and Soden, B. J.: Global Warming and the Weakening of the Tropical Circulation, J. Clim.,
760   20, 4316-4340, https://doi.org/10.1175/jcli4258.1, 2007.

761   Vincent, D. G.: The South Pacific convergence zone (SPCZ): A review, Mon. Weather Rev., 122, 1949-
762   1970, https://doi.org/10.1175/1520-0493(1994)122<1949:TSPCZA>2.0.CO;2, 1994.

763   Visioni, D., MacMartin, D. G., Kravitz, B., Boucher, O., Jones, A., Lurton, T., Martine, M., Mills, M. J.,
764   Nabat, P., Niemeier, U., Séférian, R., and Tilmes, S.: Identifying the sources of uncertainty in
765   climate model simulations of solar radiation modification with the G6sulfur and G6solar
766   Geoengineering Model Intercomparison Project (GeoMIP) simulations, Atmos. Chem. Phys.,
767   21, 10039-10063, https://doi.org/10.5194/acp-21-10039-2021, 2021.

768   Visioni, D., MacMartin, D. G., Kravitz, B., Lee, W., Simpson, I. R., and Richter, J. H.: Reduced Poleward
769   Transport Due to Stratospheric Heating Under Stratospheric Aerosols Geoengineering, Geophys.

770   Res. Lett., 47, https://doi.org/10.1029/2020gl089470, 2020.

771   Wajsowicz, R. C.: The circulation of the depth-integrated flow around an island with application to the
772   Indonesian Throughflow, J. Phys. Oceanogr., 23, 1470-1484, https://doi.org/10.1175/1520-
773   0485(1993)023<1470:TCOTDI>2.0.CO;2, 1993.

774   Wang, Q., Moore, J. C., and Ji, D.: A statistical examination of the effects of stratospheric sulfate
775   geoengineering on tropical storm genesis, Atmos. Chem. Phys., 18, 9173-9188,
776   https://doi.org/10.5194/acp-18-9173-2018, 2018.

777   Wyrtki, K.: Indonesian through flow and the associated pressure gradient, J. Geophys. Res.: Oceans, 92,
778   12941-12946, https://doi.org/10.1029/JC092iC12p12941, 1987.

779   Xia, Y D.E. Gwyther, B. Galton-Fenzi, E.A. Cougnon, A.D. Fraser, J.C. Moore, Eddy and tidal driven
780   basal melting of the Totten and Moscow University Ice Shelves, Frontiers in Marine Science,
781   10 https://doi.org/10.3389/fmars.2023.1159353 2023

782   Xie, M., Moore, J. C., Zhao, L., Wolovick, M., and Muri, H.: Impacts of three types of solar
783   geoengineering on the Atlantic Meridional Overturning Circulation, Atmos. Chem. Phys., 22,
784   4581-4597, https://doi.org/10.5194/acp-22-4581-2022, 2022.

785

786

787